PHYSICS

Resonant inelastic x-ray incarnation of Young's double-slit experiment

A. Revelli[1], M. Moretti Sala[2,3], G. Monaco[4], P. Becker[5], L. Bohatý[5], M. Hermanns[6,7,8,9], T. C. Koethe[1], T. Fröhlich[1], P. Warzanowski[1], T. Lorenz[1], S. V. Streltsov[10,11], P. H. M. van Loosdrecht[1], D. I. Khomskii[1], J. van den Brink[12], M. Grüninger[1]*

Young's archetypal double-slit experiment forms the basis for modern diffraction techniques: The elastic scattering of waves yields an interference pattern that captures the real-space structure. Here, we report on an inelastic incarnation of Young's experiment and demonstrate that resonant inelastic x-ray scattering (RIXS) measures interference patterns, which reveal the symmetry and character of electronic excited states in the same way as elastic scattering does for the ground state. A prototypical example is provided by the quasi-molecular electronic structure of insulating $Ba_3CeIr_2O_9$ with structural Ir dimers and strong spin-orbit coupling. The double "slits" in this resonant experiment are the highly localized core levels of the two Ir atoms within a dimer. The clear double-slit-type sinusoidal interference patterns that we observe allow us to characterize the electronic excitations, demonstrating the power of RIXS interferometry to unravel the electronic structure of solids containing, e.g., dimers, trimers, ladders, or other superstructures.

INTRODUCTION

Resonant inelastic x-ray scattering (RIXS) provides a powerful example of particle-wave duality in quantum mechanics. In RIXS in the particle picture, an incident x-ray photon excites an electron out of the core of an atom into an empty valence level. The highly excited atomic state that is produced in this way contains an extremely localized hole in its core, with a size of a few picometers. Subsequently, this intermediate state decays: A valence electron fills the core hole under reemission of a photon with lower photon energy than the incident one. The final excited state may correspond to, e.g., an interband, orbital, or magnetic excitation (*1*). Here, we focus on the equivalent picture of x-ray waves that are scattered via a localized intermediate state and interfere.

In the early 1990s, it was realized that even if in RIXS the scattering is inelastic and the atomic core hole is very local, the amplitudes for its creation and annihilation have to be summed up coherently when identical ions are involved over which the final excited state is delocalized (*2*–*4*). As a consequence, interference effects become possible. Specifically, in 1994, an interference pattern equivalent to Young's double-slit experiment was predicted for RIXS on diatomic molecules (*3*, *4*), an effect that, so far, has not been observed. A double-slit-like interference occurs because the RIXS intermediate state contains a single core hole that can be on either of the two atoms in the molecule (see Fig. 1). The final state exhibits an electron in an excited molecular orbital, which is delocalized over the two atoms. It corresponds to an observer without "which-path" information, i.e., one cannot tell on which atom the core hole was localized in the intermediate state. The emitted x-rays interfere and give rise to a double-slit-type sinusoidal interference pattern as a function of the momentum **q** that is transferred in the inelastic scattering process.

In a gas of diatomic molecules, the interference is blurred by orientational disorder. This complication is absent in crystalline solids with a quasi-molecular electronic structure such as insulating $Ba_3CeIr_2O_9$ (BCIO; see Fig. 2A) (*5*), an ideal model system with quasi-molecular orbitals localized on well-ordered structural dimers. As we show below, the excellent energy and momentum resolution of state-of-the-art RIXS (*6*) allows us to observe astonishingly clear interference patterns which are the unambiguous fingerprints of the symmetry of the low-energy electronic excitations.

RESULTS

We have grown single crystals of hexagonal BCIO (space group $P6_3/mmc$) by the melt-solution technique (see Materials and Methods). Each of the Ir^{4+} ions within the structural dimers formally shows a $5d^5$ configuration, with one hole in the t_{2g} shell. However, the nearest-neighbor Ir-Ir distance of 2.5 Å is even shorter than the 2.7 Å found in Ir metal. Accordingly, the intradimer Ir-Ir hopping is large, driving the formation of quasi-molecular orbitals with large bonding-antibonding splitting. It should be stressed that this situation is very different from the case of a single Ir^{4+} site, where strong spin-orbit coupling ($\lambda \approx 0.4 - 0.5$ eV) splits up the local t_{2g} manifold and yields spin-orbit–entangled $j = 1/2$ moments (see Fig. 2B). Prominent examples showing rich $j = 1/2$ physics are Sr_2IrO_4 (*7*–*10*) and Na_2IrO_3 (*11*–*13*).

There are two limiting scenarios for an effective description of the electronic structure of BCIO, i.e., for the character of the bonding and antibonding quasi-molecular orbitals. For strong spin-orbit coupling, (anti-)bonding states can be formed from spin-orbit-entangled $j = 1/2$ states (see Fig. 2D). However, a large Ir-Ir hopping may quench the $j = 1/2$ moments, as has been discussed for Na_2IrO_3 (*14*, *15*). In this case, the crystal-field-split t_{2g} orbitals provide a more appropriate basis for the formation of (anti-)bonding states (see Fig. 2C). As will become clear in the following, these substantial differences in the Ir 5d orbitals can be highlighted and quantified by RIXS interferometry, i.e., RIXS measurements of **q**-dependent interference patterns, which reveal the symmetry and character of the excited states.

[1]II. Physikalisches Institut, Universität zu Köln, Zülpicher Strasse 77, D-50937 Köln, Germany. [2]European Synchrotron Radiation Facility, BP 220, F-38043 Grenoble Cedex, France. [3]Dipartimento di Fisica, Politecnico di Milano, Piazza Leonardo da Vinci 32, I-20133 Milano, Italy. [4]Dipartimento di Fisica, Università di Trento, via Sommarive 14, 38123 Povo (TN), Italy. [5]Abteilung Kristallographie, Institut für Geologie und Mineralogie, Zülpicher Strasse 49b, D-50674 Köln, Germany. [6]Institut für Theoretische Physik, Universität zu Köln, Zülpicher Strasse 77, D-50937 Köln, Germany. [7]Department of Physics, University of Gothenburg, SE-412 96 Gothenburg, Sweden. [8]Department of Physics, Stockholm University, AlbaNova University Center, SE-106 91 Stockholm, Sweden. [9]Nordita, KTH Royal Institute of Technology and Stockholm University, Roslagstullsbacken 23, SE-106 91 Stockholm, Sweden. [10]M.N. Mikheev Institute of Metal Physics, Ural Branch, Russian Academy of Sciences, 620137 Ekaterinburg, Russia. [11]Ural Federal University, Mira Street 19, 620002 Ekaterinburg, Russia. [12]Institute for Theoretical Solid State Physics, IFW Dresden, Helmholtzstrasse 20, 01069 Dresden, Germany.
*Corresponding author. Email: grueninger@ph2.uni-koeln.de

Figure 3A depicts high-resolution RIXS spectra of BCIO for a fixed incident energy tuned to the Ir L_3 edge (2p → 5d) (see Materials and Methods), which resonantly enhances inelastic scattering from intra-t_{2g} excitations. With a 5d $t_{2g} - e_g^{\sigma}$ splitting of about 3 eV, the observed features between 0.5 and 1.5 eV, labeled α, β, and γ, can safely be attributed to intra-t_{2g} excitations. The absence of dispersion strongly supports a local character (see Supplementary Text). The spectra do not display the characteristic feature of individual $j = 1/2$ moments, the narrow spin-orbit exciton peaking at about 1.5λ. A textbook example of the latter is found in isostructural $Ba_3Ti_{2.7}Ir_{0.3}O_9$, where the small Ir content prevents dimer formation (see Supplementary Text).

The crucial observation is that the integrated intensity of the observed features shows the characteristic two-beam interference pattern (*3*, *4*), i.e., a pronounced sinusoidal oscillation as a function of q_c, the component of the transferred momentum **q** parallel to the dimer axis (see Fig. 3B). The period $2Q = 2\pi/d$ yields $d = 2.530(8)$ Å at $T = 20$ K, which is in very good agreement with the Ir-Ir distance of 2.5361(7) Å determined at 300 K by x-ray diffraction (see Supplementary Text). Note that $Q = 2.914 \cdot 2\pi/c$ is incommensurate with the reciprocal lattice vector $2\pi/c$, where c denotes the lattice constant. A clear dichotomy with respect to even/odd Q is also evident from the RIXS spectra in Fig. 3A. Even without further knowledge of the underlying microscopic physics, the observed interference pattern with a period given by the Ir-Ir distance is an unmistakable proof of the double-slit-type RIXS process originating from the quasi-molecular orbital character of the investigated states.

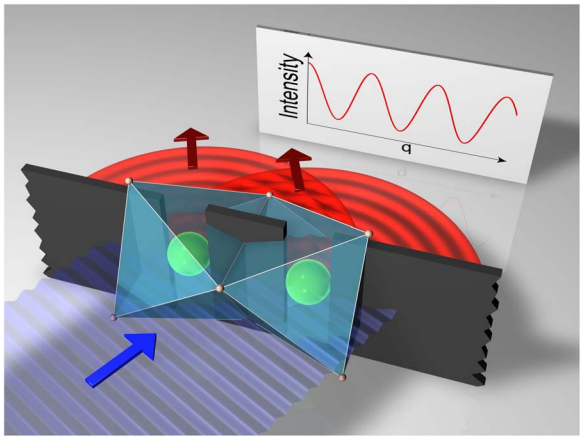

Fig. 1. Double-slit-type RIXS interferometry for an Ir_2O_9 bioctahedron. The incident plane wave (blue) resonantly excites a core electron on one of two equivalent Ir sites at $\mathbf{r}_1$ and $\mathbf{r}_2$. This intermediate state decays to a quasi-molecular final state, which is delocalized over both sites, i.e., without which-path information. The emitted x-rays interfere with each other, giving rise to a double-slit-type sinusoidal interference pattern as a function of the transferred momentum **q**, which points along $\mathbf{r}_1 - \mathbf{r}_2$.

DISCUSSION

The most remarkable feature of RIXS interferometry is the ability to determine the symmetry of the low-energy excitations and thus to distinguish between the two limiting scenarios sketched in Fig. 2 (C and D). The symmetry is encoded in the phase of the interference pattern. Young's canonical elastic double-slit experiment gives a maximum for $\mathbf{q} = 0$, which is equivalent to the $\cos^2(qd/2)$ dependence observed for peak γ (see Fig. 3C). The cosine denotes the Fourier transform of the double slit, i.e., its structure factor. Strikingly, features α and β show a $\sin^2(qd/2)$ modulation. In our experiment on structural dimers with a bonding singlet ground state, the $\sin^2(qd/2)$ or $\cos^2(qd/2)$ behavior of the observed RIXS features reflects the bonding or antibonding character of the corresponding excited-state wave functions, respectively. This behavior embodies the simple dipole selection rules for both the absorption and reemission processes (see Supplementary Text). The

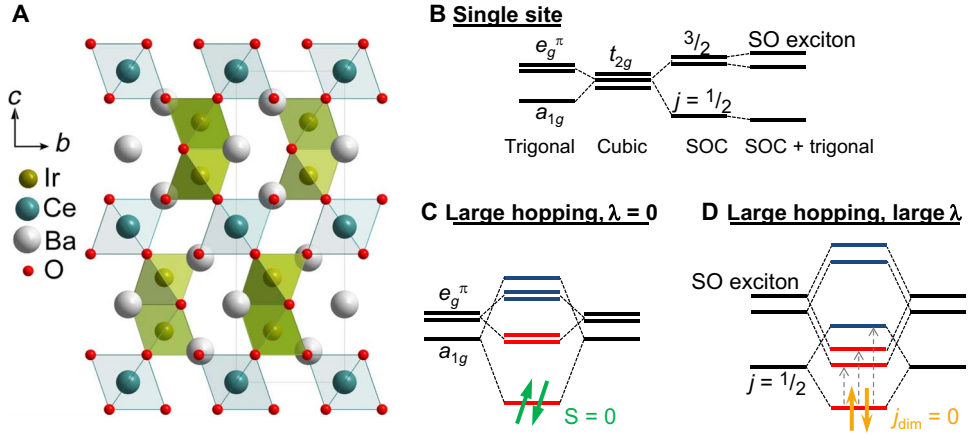

Fig. 2. Crystal structure and quasi-molecular orbitals of $Ba_3CeIr_2O_9$. (**A**) Layers of Ir_2O_9 bioctahedra (light green) are sandwiched between Ce layers. The two Ir ions are displaced by 2.5 Å along c. (**B**) All sketches refer to the hole representation. For a single Ir^{4+} site, the t_{2g} level is split by a trigonal crystal field Δ_{CF} into a_{1g} and e_g^{π} orbitals or by spin-orbit coupling λ (SOC) into $j = 1/2$ and 3/2 states. Real materials show both λ and Δ_{CF}, which yields three distinct orbitals (right), where the two excited states are called spin-orbit exciton. (**C** and **D**) Sketches of quasi-molecular orbitals for two Ir^{4+} sites with dominant hopping and small Δ_{CF}. Bonding and antibonding levels (*27*, *29*) are depicted in red and blue, respectively. In (C), $\lambda = 0$, as on the left-hand side in (B). The ground state is the a_{1g}^2 spin singlet with total $S = 0$ (green arrows). In (D), both spin-orbit coupling and hopping are large, as on the right-hand side in (B). Bonding and antibonding states are formed from local j states. The ground state is a total $j_{dim} = 0$ singlet built from two $j = 1/2$ states (orange arrows). Vertical dashed arrows indicate the three lowest excitations, which correspond to peaks α, β, and γ in the RIXS spectra. Rigorous calculations of the eigenstates (see Materials and Methods and Supplementary Text) support that the simple picture plotted in (D) contains the essential character of the low-energy excitations.

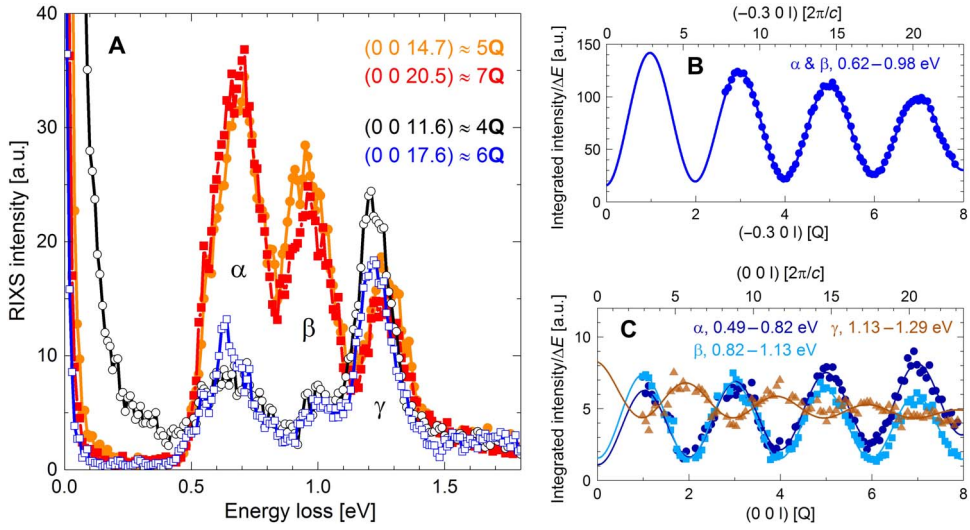

Fig. 3. RIXS data of intra-t_{2g} excitations in BCIO. (**A**) High-resolution RIXS spectra at T = 20 K for different transferred momenta **q** = (0 0 mQ) with integer m and $Q = \pi/d = 2.914 \cdot 2\pi/c$, where d and c denote the intradimer Ir-Ir distance and the lattice constant, respectively. The spectra show a pronounced even/odd behavior with respect to m, reflecting the sinusoidal **q** dependence. Note that the elastic peak is suppressed in π polarization for a scattering angle of 2θ = 90° and that the data for 4Q to 7Q were measured at 2θ = 52°, 67°, 83°, and 101°, respectively. Accordingly, the elastic peak is strongest for 4Q. (**B** and **C**) Interference patterns in the RIXS intensity as a function of **q**. The data cover about 3.5 periods in Q, equivalent to more than 20 Brillouin zones (top axis). The intensity was integrated over the energy loss ranges indicated in the figure and normalized by the width ΔE of the respective energy range. Data in (B) were measured at 10 K with lower energy resolution of 0.36 eV, integrating over features α and β, to enhance the signal-to-noise ratio. The high-resolution data in (C) discriminate between the three peaks α (dark blue), β (light blue), and γ (brown). Solid lines depict fits using $a_0 e^{-a_1 l} \cdot \sin^2(\pi l/2Q + \phi) + b_0 + b_1 l$ with the parameters Q, a_0, a_1, b_0, and b_1, as well as $\phi = 0$ or $\pi/2$.

symmetry of the observed interference patterns agrees with Fig. 2D and suggests that this simplified sketch provides a valid starting point for an intuitive understanding of the three low-energy features α, β, and γ.

This assignment is corroborated by careful modeling of the Ir_2O_9 bioctahedra. We take into account spin-orbit coupling λ, hopping terms within a dimer, the trigonal crystal field Δ_{CF}, and on-site Coulomb correlations described by Hubbard U and Hund exchange J_H (see Materials and Methods). The calculated RIXS spectra and the corresponding **q**-dependent intensities (see Fig. 4) qualitatively agree with our experimental results. In particular, we reproduce the $\sin^2(qd/2)$ behavior of peaks α and β and the $\cos^2(qd/2)$ behavior of peak γ. This implies quasi-molecular orbitals that are governed by a combination of strong spin-orbit coupling $\lambda \approx 0.4 - 0.5$ eV and strong hopping ~1 eV. The hopping is about three times larger than between nearest-neighbor $j = 1/2$ moments in Sr_2IrO_4. The dominant contribution to the ground state is a dimer singlet with $j_{dim} = 0$ in which the single-site $j = 1/2$ moments occupy a bonding quasi-molecular orbital. As depicted in Fig. 2D, the two lower features α and β correspond to excitations to bonding orbitals originating from the $j = 3/2$ spin-orbit exciton, and their splitting is mainly caused by J_H and Δ_{CF}. We find that peak γ at 1.2 to 1.3 eV corresponds to the antibonding triplet excitation from the $j_{dim} = 0$ ground state to a $j_{dim} = 1$ excited state of a dimer. This j flip can be realized by both spin-flip and spin-conserving processes. The former are allowed in L-edge RIXS due to the very strong spin-orbit coupling in the 2p shell in the intermediate state. In the calculated spectra, the triplet excitation intensity is somewhat overestimated because of the neglect of the electron-hole continuum above the gap, which provides a possible decay channel for the local excitations considered here with a concomitant increase of the width.

Last, we address the envelope of the sinusoidal interference pattern. The RIXS data cover about 20 Brillouin zones. Still, the amplitude of the intensity modulation does not change strongly, at least for peaks α and β, allowing us to detect the interference pattern over a broad range of **q**. This is due to the nearly point-like nature of the effective "slits" formed by the core hole in the intermediate states (*1*), i.e., the "slit width" is negligible. The **q**-dependent envelope rather contains valuable information on the dependence of the RIXS matrix elements on the scattering geometry and thereby on the precise wave functions.

CONCLUSION

The comparison of theory and experiment on BCIO shows that the quasi-molecular orbitals, delocalized over the two Ir sites of a dimer, give rise to the RIXS interference effect, which was predicted almost 25 years ago as an inelastic incarnation of Young's double-slit experiment. Conceptually different interference effects as a function of energy but not of **q** arise if energetically different intermediate states—located on the same site—contribute coherently (*16*, *17*). In contrast, our experiment realizes the genuine spatial double-slit setup: A photon scatters inelastically on one of two dimer sites. Previously, this was discussed in the context of dimers in VO_2 (*18*), but only a single value of **q** was analyzed because of the limited momentum transfer available in the soft x-ray range. Similarly, studies of magnons in the bilayer compound $Sr_3Ir_2O_7$ (*19*) and of stripes in nickelates and cuprates (*20*) addressed only a few values of **q**. Coverage of a broad range of **q** fully reveals the interference character and allowed us to unravel the symmetry and character of electronic dimer excitations in BCIO. These results demonstrate the potential of this interference method to probe the electronic structure of materials containing well-defined structural units such as dimers, trimers, or heptamers (*21*), as well as structures in which the carriers are "localized" only in one direction, e.g., bilayers or ladders. More specifically, our results suggest that RIXS interferometry is ideally suited to explore the role of molecular orbitals in the spin-liquid candidate $Ba_3InIr_2O_9$ with In^{3+} ions and three holes per dimer (*22*), as well as to search for Majorana fermions in iridate candidates for

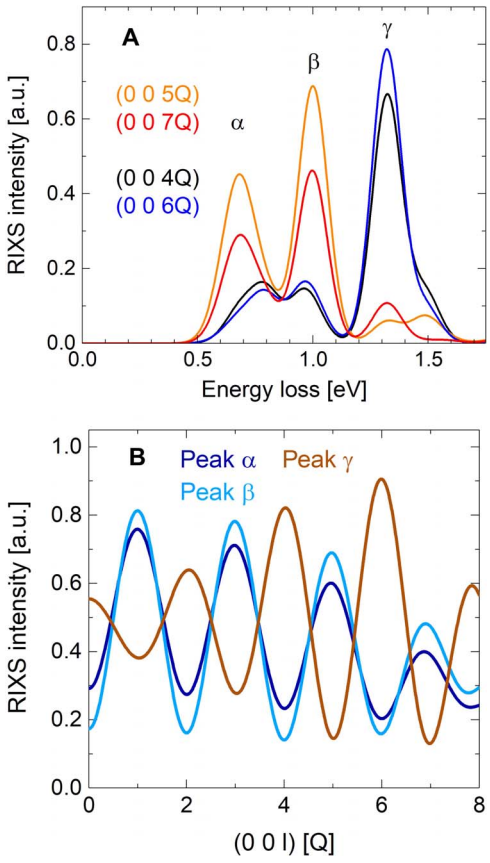

Fig. 4. Calculated RIXS data of BCIO. (**A**) Calculated RIXS spectra are plotted for the same **q** values as the experimental data in Fig. 3, reproducing peaks α, β, and γ, as well as their pronounced even/odd behavior with respect to *Q* (see Supplementary Text for more details). (**B**) Interference patterns as a function of **q** for peaks α, β, and γ, which have to be compared with the experimental result depicted in Fig. 3C. Parameters are $t_{a_{1g}}$ = 1.1 eV, $t_{e_g^\pi}$ = 0.5 eV, *U* = 1.0 eV, J_H = 0.3 eV, Δ_{CF} = −0.2 eV, and λ = 0.45 eV (see Supplementary Text).

a Kitaev spin liquid (*9*). The latter quantum state lives on tricoordinated lattices; still, spin correlations are restricted to nearest neighbors. Majorana fermion excitations are thus expected to show an interference pattern that is closely related to the case of dimers in BCIO. In general, RIXS interferometry will prove to be an efficient tool for studying the symmetry and character of excited states in complex materials.

MATERIALS AND METHODS

Crystal growth and characterization

The $Ba_3MIr_2O_9$ family with the hexagonal (6H)-$BaTiO_3$ structure is formed for a wide variety of di-, tri-, or tetravalent *M* ions (*5*, *23*–*25*). The valence states of *M* = Ce^{4+} and Ti^{4+} yield $5d^5$ Ir^{4+} ions. Single crystals of $Ba_3CeIr_2O_9$ and $Ba_3Ti_{2.7}Ir_{0.3}O_9$ have been grown by the melt-solution technique and spontaneous nucleation. Using stoichiometric amounts of $BaCO_3$, CeO_2, and IrO_2 for the growth of $Ba_3CeIr_2O_9$ and $BaCO_3$, TiO_2, and IrO_2 in a ratio of 3:2:1 in the case of $Ba_3Ti_{2.7}Ir_{0.3}O_9$, and in both cases an addition of $BaCl_2 \cdot 2H_2O$, hexagonal prismatic crystals of about 2-mm size were grown within growth periods of 4 weeks. The crystals were mechanically separated from the flux, washed with cold H_2O, and characterized by x-ray diffraction, energy-dispersive x-ray analysis, and magnetization measurements.

RIXS measurements

RIXS measurements at the Ir L_3 edge were performed on the ID20 beamline at ESRF (*6*). We used an incident energy of 11.2155 keV for *M* = Ce and 11.2150 keV for *M* = Ti to maximize the resonantly enhanced RIXS intensity of the intra-t_{2g} excitations. An overall energy resolution of 27 meV was obtained by combining a Si(844) backscattering monochromator and *R* = 2 m Si(844) spherical diced crystal analyzers (*26*). These analyzers make the RIXS setup partially dispersive, i.e., one image on the pixelated detector covers an energy range of approximately 360 meV. Accordingly, the RIXS spectra of Fig. 3A were measured by scanning the energy at constant **q**, while the data in Fig. 3C were collected by scanning **q** at constant energy. The data in Fig. 3B were measured with a lower resolution of 0.36 eV using a Si(311) channel-cut in place of the Si(844) backscattering monochromator to enhance the signal-to-noise ratio. For both *M* = Ce and *M* = Ti, RIXS measurements were performed on polished (0 0 1) surfaces with the *c* axis in the horizontal scattering plane and the *a* axis along the vertical direction. The incident photons were π polarized. Samples were cooled using a continuous-flow He cryostat.

Theory

The sketch in Fig. 2D provides a simplified but intuitive picture of the low-energy excitations. For the simulation of the RIXS spectra, we calculated all 66 eigenstates for two t_{2g} holes on two Ir sites of an Ir_2O_9 bioctahedron via exact diagonalization. We started from the Hamiltonian for a single Ir site, taking into account spin-orbit coupling $\lambda \mathbf{S} \cdot \mathbf{L}$ and the trigonal crystal field, $\Delta_{CF} L_z^2$. The on-site Coulomb repulsion between carriers with different spins in the same or in different orbitals is given by *U* and $U - 2J_H$, respectively, and the interaction Hamiltonian reads

$$H_C = U\sum_{i,\alpha} n_{i\alpha\uparrow} n_{i\alpha\downarrow} + \frac{1}{2}(U - 3J_H) \sum_{i,\sigma,\alpha\neq\alpha'} n_{i\alpha\sigma} n_{i\alpha'\sigma} + (U - 2J_H) \sum_{i,\alpha\neq\alpha'} n_{i\alpha\uparrow} n_{i\alpha'\downarrow} + (U - 2J_H) \sum_i \left(15 - 5\sum_{\alpha,\sigma} n_{i\alpha\sigma}\right)$$

where $n_{i\alpha\sigma}$ is the number operator for the t_{2g} orbitals $\alpha \in \{a_{1g}, e_g^{\pi+}, e_g^{\pi-}\}$ (*27*) at site *i* with $\sigma \in \{\uparrow, \downarrow\}$. In addition, we considered the hopping interactions $t_{a_{1g}}$ and $t_{e_g^\pi}$ between two Ir sites.

The two octahedra forming an Ir_2O_9 bioctahedron are rotated by 180° with respect to each other around the trigonal *z* axis (see Fig. 2A and fig. S1). This causes a sign change of the *xz* and *yz* orbitals in one of the two octahedra, which affects the selection rules of excitations involving the e_g^π orbitals (*27*). For the calculation of the RIXS spectra, we considered the RIXS matrix elements for single-particle excitations between all 66 states in the dipole approximation for both absorption and reemission. As typical for t_{2g}^5 iridates (*28*), we neglected multiplet effects between the intermediate-state $2p_{3/2}$ core hole and 5d holes, which considerably simplifies the calculation. It is motivated for a t_{2g}^5 configuration by the full t_{2g} shell in the intermediate state, neglecting the e_g^σ holes. Note, however, that spin-orbit coupling mixes e_g^π and e_g^σ levels. Moreover, this approximation is not fully valid for quasi-molecular orbitals delocalized over two Ir sites, where states with two holes on the same site contribute. For comparison with the experiment, one has to add the RIXS intensities of the two layers of bioctahedra present in $Ba_3CeIr_2O_9$ (see Fig. 2A), which, for the present geometry, is equivalent to adding intensities for

$+q_c$ and $-q_c$. Last, RIXS spectra were calculated for certain q_c values by assuming Gaussian line shape with a fixed width.

SUPPLEMENTARY MATERIALS

Supplementary material for this article is available at http://advances.sciencemag.org/cgi/content/full/5/1/eaav4020/DC1

Supplementary Text

Fig. S1. Sample of $Ba_3CeIr_2O_9$ used for single-crystal x-ray diffraction (left) and sketch of an Ir_2O_9 bioctahedron with face-sharing octahedra (right).

Fig. S2. RIXS spectra of $Ba_3Ti_{2.7}Ir_{0.3}O_9$.

Fig. S3. Absence of dispersion in the RIXS spectra.

Fig. S4. RIXS spectra calculated with reduced width.

Table S1. Structural parameters determined by x-ray diffractometry.

References (*30*–*35*)

REFERENCES AND NOTES

1. L. J. P. Ament, M. van Veenendaal, T. P. Devereaux, J. P. Hill, J. van den Brink, Resonant inelastic x-ray scattering studies of elementary excitations. *Rev. Mod. Phys.* **83**, 705 (2011).
2. Y. Ma, X-ray absorption, emission, and resonant inelastic scattering in solids. *Phys. Rev. B* **49**, 5799 (1994).
3. Y. Ma, M. Blume, Interference of fluorescence x rays and coherent excitation of core levels. *Rev. Sci. Instr.* **66**, 1543 (1995).
4. F. Gel'mukhanov, H. Ågren, Resonant inelastic x-ray scattering with symmetry-selective excitation. *Phys. Rev. A* **49**, 4378 (1994).
5. Y. Doi, Y. Hinatsu, The structural and magnetic characterization of 6H-perovskite-type oxides $Ba_3LnIr_2O_9$ (Ln = Y, lanthanides). *J. Phys. Condens. Matter* **16**, 2849 (2004).
6. M. Moretti Sala, K. Martel, C. Henriquet, A. Al Zein, L. Simonelli, C. J. Sahle, H. Gonzalez, M.-C. Lagier, C. Ponchut, S. Huotari, R. Verbeni, M. Krisch, G. Monaco, A high-energy-resolution resonant inelastic X-ray scattering spectrometer at ID20 of the European Synchrotron Radiation Facility. *J. Synchrotron. Rad.* **25**, 580–591 (2018).
7. B. J. Kim, H. Jin, S. J. Moon, J.-Y. Kim, B.-G. Park, C. S. Leem, J. Yu, T. W. Noh, C. Kim, S.-J. Oh, J.-H. Park, V. Durairaj, G. Cao, E. Rotenberg, Novel $J_{\text{eff}} = 1/2$ Mott state induced by relativistic spin-orbit coupling in Sr_2IrO_4. *Phys. Rev. Lett.* **101**, 076402 (2008).
8. B. J. Kim, H. Ohsumi, T. Komesu, S. Sakai, T. Morita, H. Takagi, T. Arima, Phase-sensitive observation of a spin-orbital Mott state in Sr_2IrO_4. *Science* **323**, 1329–1332 (2009).
9. J. G. Rau, E. K.-H. Lee, H.-Y. Kee, Spin-orbit physics giving rise to novel phases in correlated systems: Iridates and related materials. *Annu. Rev. Condens. Matter Phys.* **7**, 195–221 (2016).
10. J. Kim, D. Casa, M. H. Upton, T. Gog, Y.-J. Kim, J. F. Mitchell, M. van Veenendaal, M. Daghofer, J. van den Brink, G. Khaliullin, B. J. Kim, Magnetic excitation spectra of Sr_2IrO_4 probed by resonant inelastic X-ray scattering: Establishing links to cuprate superconductors. *Phys. Rev. Lett.* **108**, 177003 (2012).
11. J. Chaloupka, G. Jackeli, G. Khaliullin, Kitaev-Heisenberg model on a honeycomb lattice: Possible exotic phases in iridium oxides A_2IrO_3. *Phys. Rev. Lett.* **105**, 027204 (2010).
12. V. M. Katukuri, S. Nishimoto, V. Yushankhai, A. Stoyanova, H. Kandpal, S. Choi, R. Coldea, I. Rousochatzakis, L. Hozoi, J. van den Brink, Kitaev interactions between $j = 1/2$ moments in honeycomb Na_2IrO_3 are large and ferromagnetic: Insights from ab initio quantum chemistry calculations. *New J. Phys.* **16**, 013056 (2014).
13. H. Gretarsson, J. P. Clancy, X. Liu, J. P. Hill, E. Bozin, Y. Singh, S. Manni, P. Gegenwart, J. Kim, A. H. Said, D. Casa, T. Gog, M. H. Upton, H.-S. Kim, J. Yu, V. M. Katukuri, L. Hozoi, J. van den Brink, Y.-J. Kim, Crystal-field splitting and correlation effect on the electronic structure of A_2IrO_3. *Phys. Rev. Lett.* **110**, 076402 (2013).
14. I. I. Mazin, H. O. Jeschke, K. Foyevtsova, R. Valentí, D. I. Khomskii, Na_2IrO_3 as a molecular orbital crystal. *Phys. Rev. Lett.* **109**, 197201 (2012).
15. K. Foyevtsova, H. O. Jeschke, I. I. Mazin, D. I. Khomskii, R. Valentí, Ab initio analysis of the tight-binding parameters and magnetic interactions in Na_2IrO_3. *Phys. Rev. B* **88**, 035107 (2013).
16. L. A. Wray, S.-W. Huang, Y. Xia, M. Z. Hasan, C. Mathy, H. Eisaki, Z. Hussain, Y.-D. Chuang, Experimental signatures of phase interference and subfemtosecond time dynamics on the incident energy axis of resonant inelastic x-ray scattering. *Phys. Rev. B* **91**, 035131 (2015).
17. A. Pietzsch, Y.-P. Sun, F. Hennies, Z. Rinkevicius, H. O. Karlsson, T. Schmitt, V. N. Strocov, J. Andersson, B. Kennedy, J. Schlappa, A. Föhlisch, J.-E. Rubensson, F. Gel'mukhanov, Spatial quantum beats in vibrational resonant inelastic soft x-ray scattering at dissociating states in oxygen. *Phys. Rev. Lett.* **106**, 153004 (2011).
18. H. He, A. X. Gray, P. Granitzka, J. W. Jeong, N. P. Aetukuri, R. Kukreja, L. Miao, S. A. Breitweiser, J. Wu, Y. B. Huang, P. Olalde-Velasco, J. Pelliciari, W. F. Schlotter, E. Arenholz, T. Schmitt, M. G. Samant, S. S. P. Parkin, H. A. Dürr, L. A. Wray, Measurement of collective excitations in VO_2 by resonant inelastic x-ray scattering. *Phys. Rev. B* **94**, 161119(R) (2016).
19. M. Moretti Sala, V. Schnells, S. Boseggia, L. Simonelli, A. Al-Zein, J. G. Vale, L. Paolasini, E. C. Hunter, R. S. Perry, D. Prabhakaran, A. T. Boothroyd, M. Krisch, G. Monaco, H. M. Rønnow, D. F. McMorrow, F. Mila, Evidence of quantum dimer excitations in $Sr_3Ir_2O_7$. *Phys. Rev. B* **92**, 024405 (2015).
20. W. Schülke, C. Sternemann, Charge excitations in stripe-ordered $La_{5/3}Sr_{1/3}NiO_4$ and $La_{15/8}Ba_{1/8}CuO_4$: Interpretation of the anomalous momentum transfer dependence via fluorescence interferometry. *Phys. Rev. B* **84**, 085143 (2011).
21. S. V. Streltsov, D. I. Khomskii, Orbital physics in transition metal compounds: New trends. *Physics-Uspekhi* **60**, 1121 (2017).
22. T. Dey, M. Majumder, J. C. Orain, A. Senyshyn, M. Prinz-Zwick, S. Bachus, Y. Tokiwa, F. Bert, P. Khuntia, N. Büttgen, A. A. Tsirlin, P. Gegenwart, Persistent low-temperature spin dynamics in the mixed-valence iridate $Ba_3InIr_2O_9$. *Phys. Rev. B* **96**, 174411 (2017).
23. T. Sakamoto, Y. Doi, Y. Hinatsu, Crystal structures and magnetic properties of 6H-perovskite-type oxides $Ba_3MIr_2O_9$ (M = Mg, Ca, Sc, Ti, Zn, Sr, Zr, Cd and In). *J. Solid State Chem.* **179**, 2595–2601 (2006).
24. T. Dey, A. V. Mahajan, P. Khuntia, M. Baenitz, B. Koteswararao, F. C. Chou, Spin-liquid behavior in $J_{\text{eff}} = 1/2$ triangular lattice compound $Ba_3IrTi_2O_9$. *Phys. Rev. B* **86**, 140405(R) (2012).
25. R. Kumar, D. Sheptyakov, P. Khuntia, K. Rolfs, P. G. Freeman, H. M. Rønnow, T. Dey, M. Baenitz, A. V. Mahajan, $Ba_3M_xTi_{3-x}O_9$ (*M* = Ir, Rh): A family of 5*d*/4*d*-based diluted quantum spin liquids. *Phys. Rev. B* **94**, 174410 (2016).
26. M. Moretti Sala, C. Henriquet, L. Simonelli, R. Verbeni, G. Monaco, High energy-resolution set-up for Ir L_3 edge RIXS experiments. *J. Electron Spectrosc. Relat. Phenom.* **188**, 150–154 (2013).
27. D. I. Khomskii, K. I. Kugel, A. O. Sboychakov, S. V. Streltsov, Role of local geometry in the spin and orbital structure of transition metal compounds. *J. Exp. Theor. Phys.* **122**, 484–498 (2016).
28. L. J. P. Ament, G. Khaliullin, J. van den Brink, Theory of resonant inelastic x-ray scattering in iridium oxide compounds: Probing spin-orbit-entangled ground states and excitations. *Phys. Rev. B* **84**, 020403(R) (2011).
29. S. V. Streltsov, D. I. Khomskii, Covalent bonds against magnetism in transition metal compounds. *Proc. Natl. Acad. Sci. U.S.A.* **113**, 10491–10496 (2016).
30. J. Rodríguez-Carvajal, Recent advances in magnetic structure determination by neutron powder diffraction. *Physica B* **192**, 55–69 (1993).
31. V. Petříček, M. Dušek, L. Palatinus, Crystallographic computing system JANA2006: General features. *Z. Kristallogr.* **229**, 345–352 (2014).
32. M. Rossi, M. Retegan, C. Giacobbe, R. Fumagalli, A. Efimenko, T. Kulka, K. Wohlfeld, A. I. Gubanov, M. Moretti Sala, Possibility to realize spin-orbit-induced correlated physics in iridium fluorides. *Phys. Rev. B* **95**, 235161 (2017).
33. Y. Sizyuk, C. Price, P. Wölfle, N. B. Perkins, Importance of anisotropic exchange interactions in honeycomb iridates: Minimal model for zigzag antiferromagnetic order in Na_2IrO_3. *Phys. Rev. B* **90**, 155126 (2014).
34. B. H. Kim, G. Khaliullin, B. I. Min, Electronic excitations in the edge-shared relativistic Mott insulator: Na_2IrO_3. *Phys. Rev. B* **89**, 081109(R) (2014).
35. J. P. Perdew, K. Burke, M. Ernzerhof, Generalized gradient approximation made simple. *Phys. Rev. Lett.* **77**, 3865–3868 (1996).

Acknowledgments: We gratefully acknowledge fruitful discussions with M. Braden, I. Mazin, and S. Trebst. **Funding:** This project was funded by the Deutsche Forschungsgemeinschaft (DFG; German Research Foundation)—project numbers 277146847 and 247310070—CRC 1238 (projects A02, B01, B02, B03, and C02) and CRC 1143 (project A05), respectively. The work of S.V.S. was supported by the Russian Science Foundation through project 17-12-01207.

Author contributions: A.R., M.M.S., G.M., P.H.M.v.L., J.v.d.B., and M.G. conceived the experiment. A.R., M.M.S., G.M., T.C.K., P.H.M.v.L., and M.G. carried out the experiment at ESRF. A.R. and M.G. analyzed the experimental data. M.H., S.V.S., and M.G. performed the theoretical calculations assisted by J.v.d.B. and D.I.K. P.B. and L.B. synthesized and prepared the single crystals used for the measurements. A.R., T.F., P.W., and T.L. characterized the samples. J.v.d.B. and M.G. wrote the manuscript with contributions from all the other authors.

Competing interests: The authors declare that they have no competing interests. **Data and materials availability:** All data needed to evaluate the conclusions in the paper are present in the paper and/or the Supplementary Materials. Additional data related to this paper may be requested from the authors.

Submitted 12 September 2018
Accepted 14 December 2018
Published 18 January 2019
10.1126/sciadv.aav4020

Citation: A. Revelli, M. Moretti Sala, G. Monaco, P. Becker, L. Bohatý, M. Hermanns, T. C. Koethe, T. Fröhlich, P. Warzanowski, T. Lorenz, S. V. Streltsov, P. H. M. van Loosdrecht, D. I. Khomskii, J. van den Brink, M. Grüninger, Resonant inelastic x-ray incarnation of Young's double-slit experiment. *Sci. Adv.* **5**, eaav4020 (2019).

Resonant inelastic x-ray incarnation of Young's double-slit experiment

A. Revelli, M. Moretti Sala, G. Monaco, P. Becker, L. Bohatý, M. Hermanns, T. C. Koethe, T. Fröhlich, P. Warzanowski, T. Lorenz, S. V. Streltsov, P. H. M. van Loosdrecht, D. I. Khomskii, J. van den Brink and M. Grüninger

Sci Adv **5** (1), eaav4020.
DOI: 10.1126/sciadv.aav4020